JACS
JOURNAL OF THE AMERICAN CHEMICAL SOCIETY
pubs.acs.org/JACS
Article

Optical Cavity Manipulation and Nonlinear UV Molecular Spectroscopy of Conical Intersections in Pyrazine

Daeheum Cho,* Bing Gu,* and Shaul Mukamel*

Cite This: J. Am. Chem. Soc. 2022, 144, 7758−7767
Read Online

ABSTRACT: Optical cavities provide a versatile platform for manipulating the excited-state dynamics of molecules via strong light−matter coupling. We employ optical absorption and two-multidimensional electronic spectroscopy simulations to investigate the effect of optical cavity coupling in the nonadiabatic dynamics of photoexcited pyrazine. We observe the emergence of a novel polaritonic conical intersection (PCI) between the electronic dark state and photonic surfaces as the cavity frequency is tuned. The PCI could significantly change the nonadiabatic dynamics of pyrazine by doubling the decay rate constant of the S_2 state population. Moreover, the absorption spectrum and excited-state dynamics could be systematically manipulated by tuning the strong light−matter interaction, e.g., the cavity frequency and cavity coupling strength. We propose that a tunable optical cavity−molecule system may provide promising approaches for manipulating the photophysical properties of molecules.

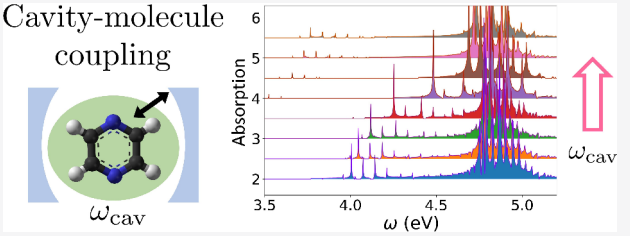

INTRODUCTION

Optical cavities provide a novel means for controlling the photochemistry and photophysics of molecules by making use of strong light−matter coupling without chemical modifications or strong external laser pulses.[1−21] Optical cavities are standing-wave light resonators that can be made of high-reflectivity mirrors (Fabry−Perot type), photonic crystals, nanomaterials, or microcircuits.[22] The coupling can be created between electronic transitions of embedded molecules and the confined cavity photon mode with the strength $g = \mu\sqrt{N}\sqrt{\frac{\hbar\omega_c}{2V\epsilon_0}}$ where μ is the transition dipole, ϵ_0 is the electric permittivity of a vacuum, N is the number of molecules in the cavity mode, which is in the vacuum state, V is volume, and ω_c is the cavity frequency. The effective coupling strength can be enhanced by increasing the molecular concentration N/V. The electronic and optical properties of molecules[2,19] are affected by vacuum fluctuations of the cavity mode. The Purcell effect, which increases the spontaneous emission rates of atoms when placed in a resonant cavity, is a notable result.[23] When the coupling strength is greater than the loss rate of the cavity mode and the decoherence rate of the molecule, the strong light−matter coupling regime is realized. The electronic or vibrational molecular degrees of freedom then combine with the cavity photon to form polaritons, which are of hybrid light−matter states. The ultrastrong coupling regime can be reached in the collective strong coupling regime with many molecules,[3,6,22,24−27] where the coupling strength is comparable to the cavity frequency $g/\omega_c \approx 0.1−0.2$.[15,28] Single-molecule strong coupling has been reported in plasmonic nanocavities where $g \approx 100$ meV and $\omega_c \approx 1.88$ eV.[29] In the single-excitation space, one major difference between many-molecule and single-molecule strong coupling is that there is a manifold of collective dark states for $N \gg 1$, which may affect the cavity-controlled chemical reactions.[30] The splitting of a single molecular resonance into a doublet of polariton states in the absorption and cavity transmission spectra[3] is a signature of strong coupling. However, for a dense electronic state manifold, it is possible to observe only a single polariton state.[31] Cavity polaritons have been shown to strongly affect the electronic, optical, and chemical properties of molecules and materials, such as increasing the conductivity of organic semiconductors,[32] reversing the selectivity of a ground-state chemical reaction,[33] improving optical nonlinearity,[6] and enabling long-range electronic and vibrational energy transfer.[27,34] These findings triggered intense theoretical studies.[1,2,19,35−39]

Herein, we investigate cavity effects on molecules undergoing conical intersections. Conical intersections (CIs) in bare molecules play an important role in many chemical and biophysical processes, including the primary event of vision and photostability of DNA molecules,[40] by providing an ultrafast nonradiative electronic decay channel for excited

Received: January 24, 2022
Published: April 11, 2022

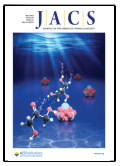

https://doi.org/10.1021/jacs.2c00921
J. Am. Chem. Soc. 2022, 144, 7758−7767

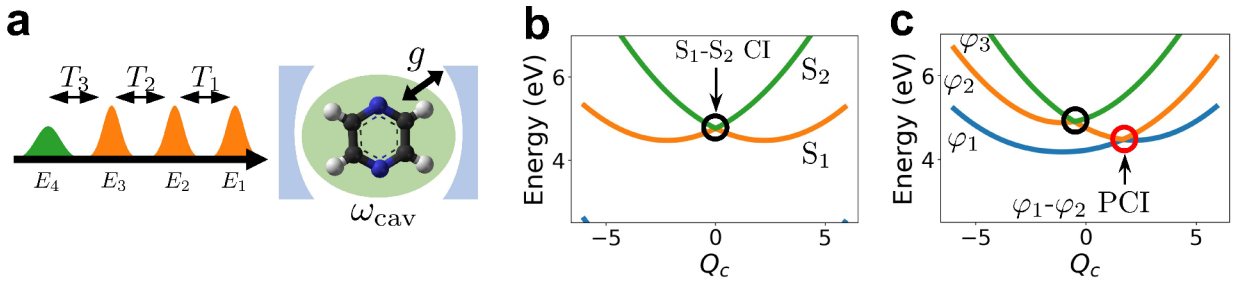

Figure 1. (a) Pulse configuration and time delays for four-wave mixing of a pyrazine molecule in a cavity, (b) 1D adiabatic electronic PES S_n of the bright (S_2) and the dark (S_1) excited states of a bare molecule along the Q_c vibrational coordinate while Q_t is fixed at −3.5 where the conical intersection occurs (the electronic ground state (S_0) is not shown). The black dark circle denotes the CI between the two excited states (S_1−S_2 CI) is marked by a black circle. (c) Example of 1D PPESs φ_n of a molecule in a cavity with cavity frequency ω_{cav} = 4.0 eV and cavity coupling strength g = 2000 cm^{-1}. The red circle denotes the novel PCI ($\varphi_1 - \varphi_2$ PCI).

molecules due to the strong electron−nuclear coupling at the crossing region. The detection and control of nonadiabatic dynamics around CIs have been extensively studied.[41−47] Various nonlinear spectroscopic techniques have been used to investigate photochemical dynamics around CIs, including monitoring state population dynamics,[48,49] transient vibrational/visible spectra,[50−53] transient absorption, photoionization spectra,[54] and (off-)resonant stimulated X-ray Raman techniques.[55] Nonadiabatic molecular dynamics occur in an optical cavity on polaritonic potential energy surfaces (PPESs), with hybrid electron−photon polaritonic states replacing the bare adiabatic potential energy surfaces. The PPESs have more features than their bare adiabatic counterparts, such as light-induced crossings and polaritonic conical intersections,[20,56,57] which can be modulated by cavity frequencies and the cavity−molecule coupling. Cavities could significantly alter the photochemistry of molecules and can be used to control photochemical reactions by molecular polaritons. Time-resolved nonlinear spectroscopic techniques are required for the real-time monitoring of ultrafast polaritonic dynamics.[58,59] Experiments in two-dimensional (2D) infrared spectroscopy have been carried out to study the relaxation dynamics of vibrational polaritons.[58,60]

We use multidimensional electronic spectroscopy to investigate the polaritonic dynamics of a pyrazine molecule coupled to a single cavity mode in this study. 2D electronic spectroscopy (2DES) provides a time-resolved ultrafast probe for dynamics in a wide variety of materials, including molecular aggregates and photosynthetic complexes.[61] We previously simulated the polaritonic dynamics and pump−probe transient absorption spectra of a single and a pair of pyrazine molecules in an optical cavity[20,21] and demonstrated that the cavity mode could split the pristine S_1/S_2 CI into two polaritonic CIs, significantly altering the internal conversion dynamics. The competition between wavepacket dynamics on the bright PPESs and dark-state surfaces determines the polaritonic dynamics of a pair of pyrazines. To monitor polaritonic dynamics in real time, multidimensional electronic spectroscopy of the polaritonic conical intersection should be useful.[21]

To simulate the 2DES of molecules in an optical cavity, we use a phase-cycling protocol in conjunction with a nonadiabatic wavepacket dynamics method. This method avoids diagonalizing the full photon−electron−nuclear Hamiltonian, which is required in perturbative simulations, and also accounts for the pulse shape without employing the impulsive limit. It entails explicitly propagating the polaritonic dynamics including the external probing laser pulses and scanning the interpulse temporal delays, i.e., coherence time T_1, population time T_2, and detection time T_3 (see Figure 1). Polaritonic dynamics is simulated by numerically exact nonadiabatic wavepacket dynamics with two vibrational modes. The phase-cycling protocol dissects the desired third-order response functions, each represented by a Liouville space pathway.[62] We investigate the optical signatures of strong coupling in the nonadiabatic polariton dynamics of photoexcited pyrazine by examining the population dynamics, PPESs, linear absorption, and photon echo spectroscopy. Our simulations demonstrate how the couplings between molecular degrees of freedom (vibrational or electronic) can be extracted from multidimensional spectroscopy by exploiting multiple electric fields.

THEORY AND COMPUTATIONAL DETAILS

Nonadiabatic Dynamics in an Optical Cavity. The Hamiltonian of a molecule in the optical cavity is given by the sum of the molecular Hamiltonian H_M, the cavity photon Hamiltonian H_C, the cavity−matter interaction H_{CM}, and the classical light−matter interaction $H_{LM}(t)$

$$H = H_M + H_C + H_{CM} + H_{LM}(t) \tag{1}$$

Pyrazine is modeled by a linear−vibronic coupling effective Hamiltonian developed in ref 63, which includes three electronic states (S_0, S_1, and S_2) and two vibrational modes that are strongly coupled to the electronic system. The ultrafast nonradiative decay is caused by a CI between S_1 and S_2. This model has been widely used to study the nonadiabatic dynamics via the CI.[40,64] The molecular Hamiltonian in the diabatic basis reads

$$H_M = \sum_{k=0,1,2} h_k|\psi_k\rangle\langle\psi_k| + \lambda Q_c(|\psi_1\rangle\langle\psi_2| + \text{H.c.}) \tag{2}$$

where $h_k = \sum_{\sigma=t,c} \hbar\Omega_\sigma(a_\sigma^\dagger a_\sigma + 1/2) + E_k + \kappa_k Q_t$ and H.c. denotes the Hermitian conjugate. Here, Ω_σ and Q_σ denote the frequency and dimensionless coordinate of the σth vibrational mode ($\sigma = c$ for the coupling mode and $\sigma = t$ for the tuning mode), respectively, $|\psi_k\rangle$ are the diabatic electronic states, E_k is its vertical excitation energy at the Franck−Condon point, κ_k are the intrastate electron−vibrational coupling constants, and λ denotes the interstate coupling strength. The parameters used for H_M are $\hbar\omega_c$ = 118 meV, $\hbar\omega_t$ = 74 meV, E_1 = 3.94 eV, E_2 = 4.84 eV, κ_1 = −105 meV, κ_2 = 149 meV, and λ = 261.6 meV. The cavity Hamiltonian is given by

https://doi.org/10.1021/jacs.2c00921
J. Am. Chem. Soc. 2022, 144, 7758−7767

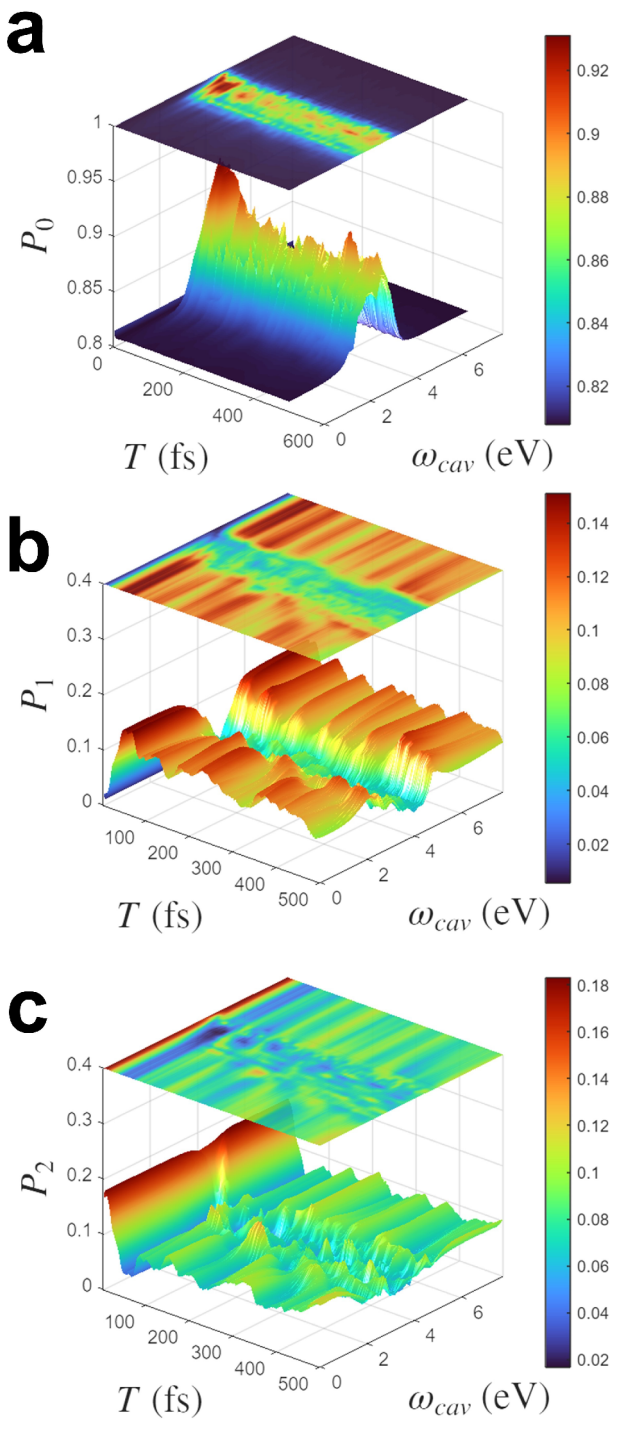

Figure 2. Nonadiabatic polaritonic dynamics for pyrazine coupled to a cavity mode with cavity photon coupling strength g = 2000 cm^{-1}. Population dynamics of electronic states (a) ψ_0 (S_0), (b) ψ_1 (S_1), and (c) ψ_2 (S_2) as functions of the time delay T and the cavity frequency ω_{cav}. The initial decay of P_0 and the initial preparation of P_2 are not shown for better visibility.

$$H_C = \hbar\omega_{cav}(a_{cav}^{\dagger}a_{cav} + 1/2) \tag{3}$$

where ω_{cav} denotes the resonance frequency of the single cavity mode and a_{cav} ($a_{cav}^{\dagger}$) denotes the annihilation (creation) operator of the cavity photon.

The cavity−molecule dipole interaction is

$$H_{CM} = \sum_{i<j} g_{ij}(\mathbf{R})(a_{cav}^{\dagger} + a_{cav})(|\psi_j\rangle\langle\psi_i| + \text{H.c.}) \tag{4}$$

where g_{ij} is the coupling strength and $\mathbf{R} = (Q_t, Q_c)$ denotes nuclear coordinates. We use the Condon approximation because the transition dipole moment matrix elements between diabatic states have a negligible dependence on the nuclear coordinates.

The nonadiabatic dynamics of pyrazine in the optical cavity are precisely simulated by numerically solving the time-dependent Schrödinger equation with a complete basis set of the full polaritonic space. A polaritonic basis function is a direct product of the diabatic electronic state $|\psi_k\rangle$, the cavity mode Fock state $|n_{cav}\rangle$, and the Fock states for the two vibrational modes $|n_c\rangle \otimes |n_t\rangle$, i.e., $|kn_{cav}n_cn_t\rangle = |\psi_k\rangle \otimes |n_{cav}\rangle \otimes |n_c\rangle \otimes |n_t\rangle$. The basis set used in all simulations is n_e = 3, n_{cav} = 2, and $n_t = n_c$ = 20, resulting in a total of 2400 basis functions in the polaritonic space. The Runge−Kutta fourth-order method was used to integrate the time-dependent Schrödinger equation for the joint light−molecule system with a time step of δt = 0.04 fs. The resulting states were used to calculate the time-dependent polarization $\langle\boldsymbol{\mu}(t)\rangle$, and the phase-cycling protocol was used to obtain the 2DES signal.

Phase-Cycling Protocol for Four-Wave Mixing Signals. Nonlinear optical signals are given by sums over Liouville pathways, representing different orders in the fields. To isolate the desired nonlinear signal, direct time-domain simulation of multidimensional signals of molecules driven by external fields requires a phase-cycling protocol.[65−68] While phase-matching is a common method for distinguishing different nonlinear pathways in experiments using noncollinear pulse configurations, phase cycling is a convenient experimental and computational alternative. We employed a nine-step phase-cycling protocol to separate the third-order photon echo contribution from the total nonadiabatic dynamics driven by three external UV pulses (refer to Supporting Information for details).

In third-order nonlinear four-wave mixing (FWM) spectroscopy, the system interacts with three electric pulses $\mathbf{E}_1$, $\mathbf{E}_2$, and $\mathbf{E}_3$ and is finally detected by the local oscillator field $\mathbf{E}_4$, which interferes with the emitted signal to generate the heterodyne signal.

$$S = \Im \int dt\langle\boldsymbol{\mu}(t)\rangle\cdot\mathbf{E}_4^*(t) \tag{5}$$

The third-order signal is given by

$$S^{(3)}(t_3, t_2, t_1) = \int dt_4 dt_3 dt_2 dt_1 R^{(3)}(t_3, t_2, t_1) \times \mathbf{E}_4(t)\mathbf{E}_3(t - t_3)\mathbf{E}_2(t - t_3 - t_2)\mathbf{E}_1(t - t_3 - t_2 - t_1) \tag{6}$$

The third-order response function $R^{(3)}(t_3, t_2, t_1)$ can be expanded in Liouville pathways (see Supporting Information Figure S1 for diagrams).

$$R^{(3)}(t_3, t_2, t_1) = \sum_{n=1}^{6} R_n(t_3, t_2, t_1) + \text{c.c.} \tag{7}$$

The 2D photon echo signal $S(\Omega_1, T_2, \Omega_3)$ is displayed by a double Fourier transform of the third-order photon echo polarization $P(T_1, T_2, T_3)$ with respect to the pulse delays T_1 and T_3 as follows:

https://doi.org/10.1021/jacs.2c00921
J. Am. Chem. Soc. 2022, 144, 7758−7767

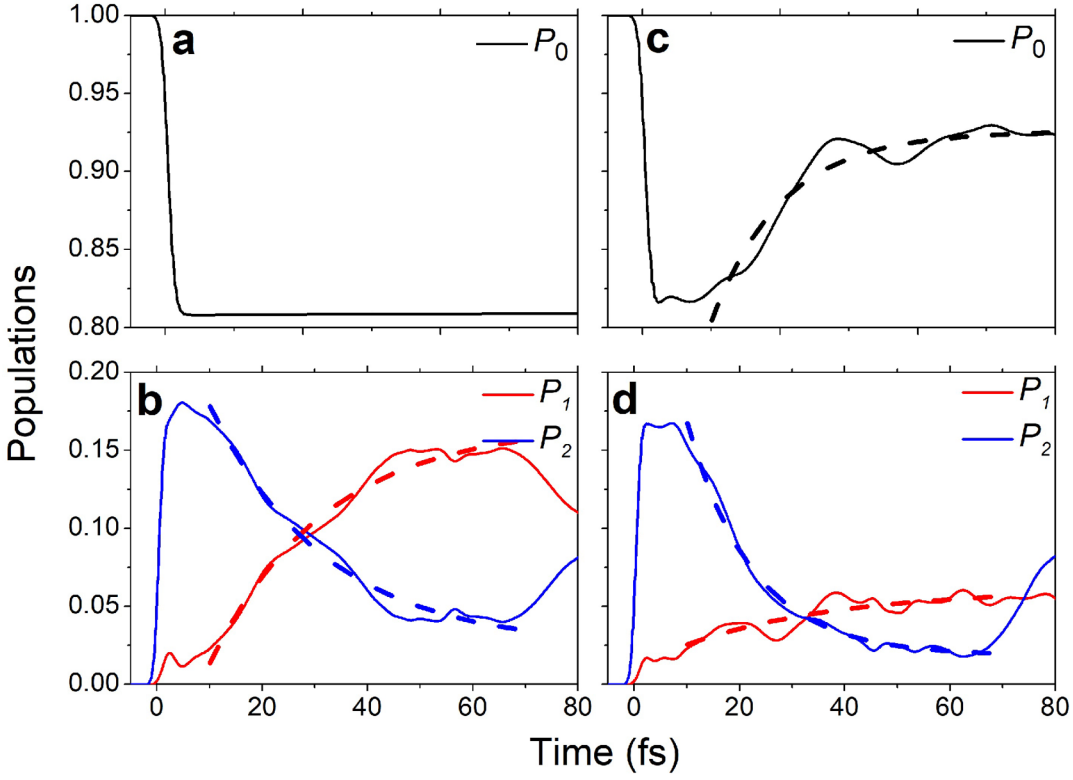

Figure 3. 1D cuts of the population dynamics of electronic states shown in Figure 2 at different cavity frequencies. (a) P_0 and (b) P_1 and P_2 of a bare molecule. (c) P_0 and (d) P_1 and P_2 of a molecule coupled to a cavity with ω_{cav} = 4 eV. Solid (dashed) line represents raw data (exponential fitting of fast decay after initial preparation).

$$S(\Omega_1, T_2, \Omega_3) = \int dT_1 \int dT_3 e^{i\Omega_1 T_1 + i\Omega_3 T_3} S(T_1, T_2, T_3) \quad (8)$$

To generate the 2DES spectra shown in Figure 7, we used 1000 sets of wavepacket dynamics with different time delays T_1 and T_3, each consisting of a simulation time of 2200 fs and a time step Δt = 0.1 au. The 2D FWM signals were generated by scanning the delays T_1 and T_3, with T_2 = 10 and 500 fs. T_1 was varied from 9.0 fs to 501.0 fs in 0.4 fs increments, and T_3 was scanned from 9.0 fs to 1001.0 fs in 0.4 fs increments. We assumed the Gaussian electric field envelopes as follows:

$$\mathbf{E}_i(t) = A \sin(\omega_i(t - t_i) + \phi_i)\exp[-(t - t_i)^2/(2\sigma_i^2)] \quad (9)$$

with an electric field strength of A = 0.01 au (3.51×10^{14} W/cm^2) for all incoming fields, central time t_i, central frequency ω_i, pulse duration σ_i, and phase ϕ_i. Time delays between pulses are given by $T_i = t_{i+1} - t_i$. The pulse central frequencies were set to ω_1 = 4.7 eV and $\omega_2 = \omega_3 = \omega_4$ = 4.0 eV with pulse durations of 10 fs at full-width at half-maximum (fwhm).

RESULTS AND DISCUSSION

Dynamics and the Absorption Spectrum. The population dynamics of adiabatic electronic states and the absorption spectra of pyrazine driven by a single electric field $\mathbf{E}_1$ with a central frequency ω_1 = 4.7 eV are first discussed. Previously, the nonadiabatic dynamics of a pyrazine molecule in a cavity, as well as its transient absorption spectroscopy, were investigated.[20] We begin by scanning the cavity frequency ω_{cav} at various coupling strengths (g) to investigate the effect of the light−matter interaction. The electronic states ψ_0 (S_0), ψ_1 (S_1), and ψ_2 (S_2) populations are plotted against the cavity frequency ω_{cav} = [0, 8] eV at the cavity−photon coupling strength g = 2000 cm^{-1} in Figure 2. In the bare molecule (g = 0 cm^{-1}), the S_2 electronic population (P_2) grows within 10 fs of initial excitation and further decays to S_1 via the S_1−S_2 CI. The initial decay of the bright excited state population P_2 is fast (~60 fs). At long times, P_2 and P_1 remain around 0.1 with several recurrences. The limited number of vibrational modes in the model Hamiltonian does not account for the further decay of the S_2 population to the S_1 surface, and the longer-time decay is accentuated by including the additional modes. Because there is no decay channel from S_1/S_2 to S_0, the electronic population of S_0 does not change during the nonadiabatic dynamics.

The coupling to the cavity photon mode significantly affects the population dynamics. Most importantly, at $\omega_{cav} \approx 4$ eV, which can couple S_0 and S_1 states via the cavity mode, the S_0 population increases significantly during nonadiabatic dynamics, as shown in Figure 2a, indicating a population transfer from S_1 and S_2 states. The cavity−molecule coupling generates a new polaritonic conical intersection (PCI) that serves as a nonadiabatic transition channel from S_1 to S_0. The PCI depicted in Figure 5 will be discussed further below. The decrease in the S_1 and S_2 populations for the cavity frequency ω_{cav} = 4 eV (Figure 2b and c) indicates that a significant S_1 population is transferred to S_0 during the nonadiabatic

Table 1. Fitting Parameters for the Early Population Dynamics to an Exponential of the Form $y = a_1 e^{-kx} + y_0$

	$P_{1,bare}$	$P_{2,bare}$	$P_{0,cav}$	$P_{1,cav}$	$P_{2,cav}$
k	0.045	0.045	0.097	0.034	0.080
a	−0.241	0.243	−0.322	−0.050	0.333

https://doi.org/10.1021/jacs.2c00921
J. Am. Chem. Soc. 2022, 144, 7758−7767

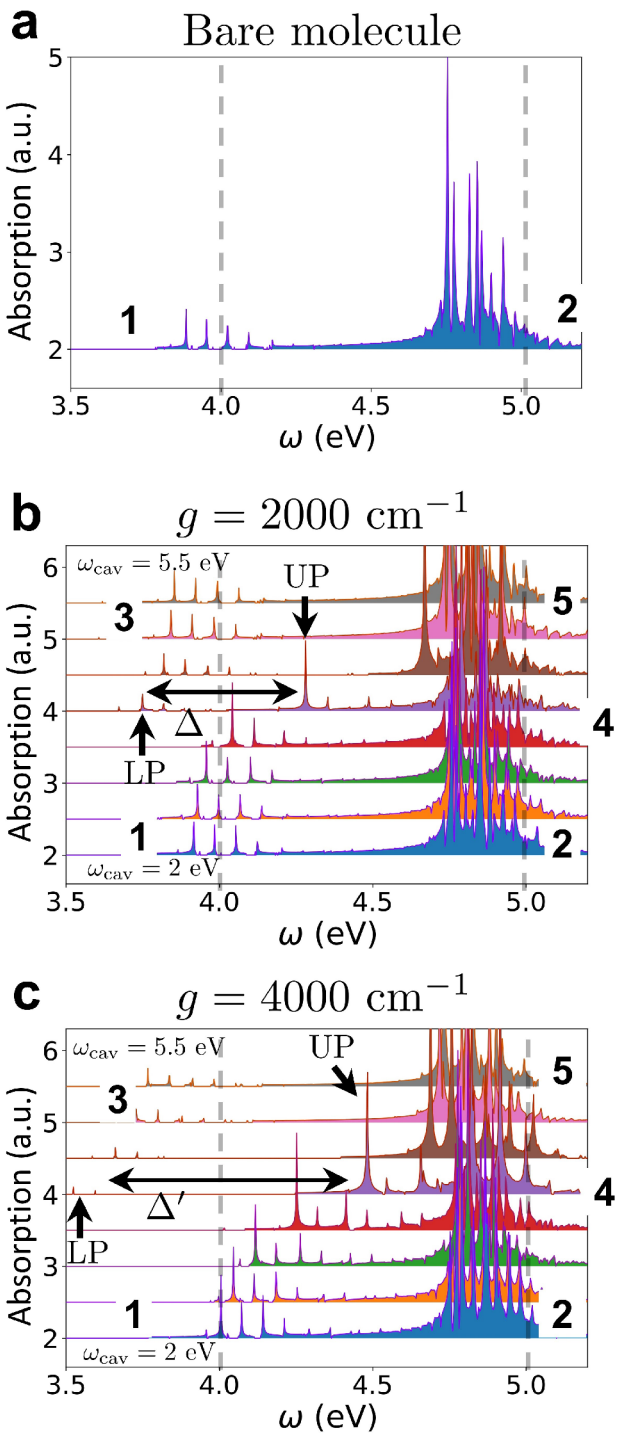

Figure 4. Absorption spectra of pyrazine (eq 5). (a) Bare molecule. A molecule in a cavity with different cavity frequencies ω_{cav} = [2, 5.5] with 0.5 eV increments at cavity photon coupling strengths (b) g = 2000 cm^{-1} and (c) g = 4000 cm^{-1}. S_1, S_2, and the PCI bands are marked as 1, 2, and 3, respectively. A blue-shift and a disappearance of the S_1 band are marked as 4. The appearance of a new S_1 band is marked as 5. The S_1 band splits into upper (UP) and lower polariton (LP) modes.

dynamics. Off-resonant cavity modes with the S_0−S_1 gap still produce a noticeable change in the S_1 and S_2 populations. This will be discussed in greater detail in the later text.

The early population dynamics are fitted to provide a quantitative analysis of the polaritonic effects. 1D cuts of S_0, S_1, and S_2 populations of a bare molecule and a molecule coupled to a cavity with ω_{cav} = 4 eV are fitted to an exponential function of the form $y = a_1 e^{-kx} + y_0$ as shown in Figure 3. $P_{n,\mathrm{bare(cav)}}$ denotes a population at the S_n surface of a bare molecule (a molecule coupled to a cavity). Table 1 collects the fitting parameters k and a. Population transfer from S_2 to S_1 in a bare molecule was found from the similar k values for $P_{1,\mathrm{bare}}$ (0.045) and $P_{2,\mathrm{bare}}$ (0.045) and opposite sign of a (−0.241 and 0.243) as shown in panels a and b. In a molecule coupled to a cavity (panels c and d), $P_{2,\mathrm{cav}}$ decays faster and to greater extent than in a bare molecule with k = 0.080 and a = 0.333, while $P_{1,\mathrm{cav}}$ increases slower and to smaller extent with k = 0.034 and a = −0.050. Importantly, it was found that a molecule−cavity coupling with ω_{cav} = 4 eV doubled the rate constant of an early decay of the $P_{2,\mathrm{cav}}$ population. The $P_{0,\mathrm{cav}}$ population rapidly increases with k = 0.097 and a = −0.322 as $P_{2,\mathrm{cav}}$ decreases.

Figure 4 shows the simulated absorption spectra of a bare molecule and a molecule coupled to a cavity mode with cavity frequency ω_{cav} = [2, 5.5] eV at g = 2000 and 4000 cm^{-1}. Cavity modes with ω_{cav} < 2 eV and ω_{cav} > 5.5 eV (not shown) do not change the absorption spectra significantly. In panel b, strong peaks originating from the $S_0 \rightarrow S_2$ transition appear in the 4.7−5.1 eV regime in a bare molecule (denoted as an S_2 band marked as 2). The S_1 band denotes weaker 3.8−4.2 eV peaks originating from the $S_0 \rightarrow S_1$ transition (marked as 1). Peak 2 is much stronger than peak 1 because the S_2 state is a bright state. Nonadiabatic effects result in a fine structure that reveals the propagation of the wavepacket and the vibrational progression on top of the electronic transitions. The fine structure in the S_2 band is more complex, whereas the fine structure in the S_1 band is simpler, indicating vibrational wavepackets along a single mode on the S_1 surface. When a pyrazine molecule is coupled to a cavity mode with g = 2000 cm^{-1} (panel b), we see interesting new features as the cavity frequency ω_{cav} increases: the S_1 absorption gradually blue-shifts as the cavity frequency increases from 3.0 to 4.5 eV and eventually merges with the S_2 band. At the S_1 absorption, another set of peaks appears (marked 3). When a cavity frequency ω_{cav} = 4 eV is resonant to the $\psi_0 - \psi_1$ energy gap, a splitting (Δ) of the S_1 band into two polaritonic modes, upper (UP) and lower (LP) polaritons, is observed. We observe a larger splitting (Δ') when the cavity−molecule coupling strength is increased to g = 4000 cm^{-1} (panel c). Besides that, we clearly see the peak shifts induced by the off-resonant (when $\omega_{cav} \neq 4$ eV) optical cavities.

The PPESs were then used to analyze the spectral features seen in Figure 4. The effect of the cavity−molecule coupling in PPESs is depicted in Figure 5. Figure 5I depicts a 3D plot of PPESs, while Figure 5II and III depict 1D cuts of PPESs along Q_c at Q_t = 0 and −3.5, respectively. The S_1−S_2 CI in a bare molecule is located at (Q_c, Q_t) = (0.0, −3.5). The wavepacket that was initially promoted to the S_2 state at (Q_c, Q_t) = (0.0, 0.0) travels to the S_1−S_2 CI to relax to the S_1 surface. The ground (φ_0) and the first excited (φ_1) polaritonic surfaces for the low cavity frequency ω_{cav} = 2 eV shown in Figure 5b are primarily caused by the coupling between a cavity mode and the electronic ground state. The states φ_0 and φ_1 have electronic and photonic characters, respectively. The electronic S_1 and S_2 characters dominate the second (φ_2) and the third (φ_3) excited polaritonic surfaces, respectively. However, there is no conical intersection between the φ_1 and φ_2. Only the S_1−S_2 CI, which can also be called φ_2−φ_3 CI, but its character is

https://doi.org/10.1021/jacs.2c00921
J. Am. Chem. Soc. 2022, 144, 7758−7767

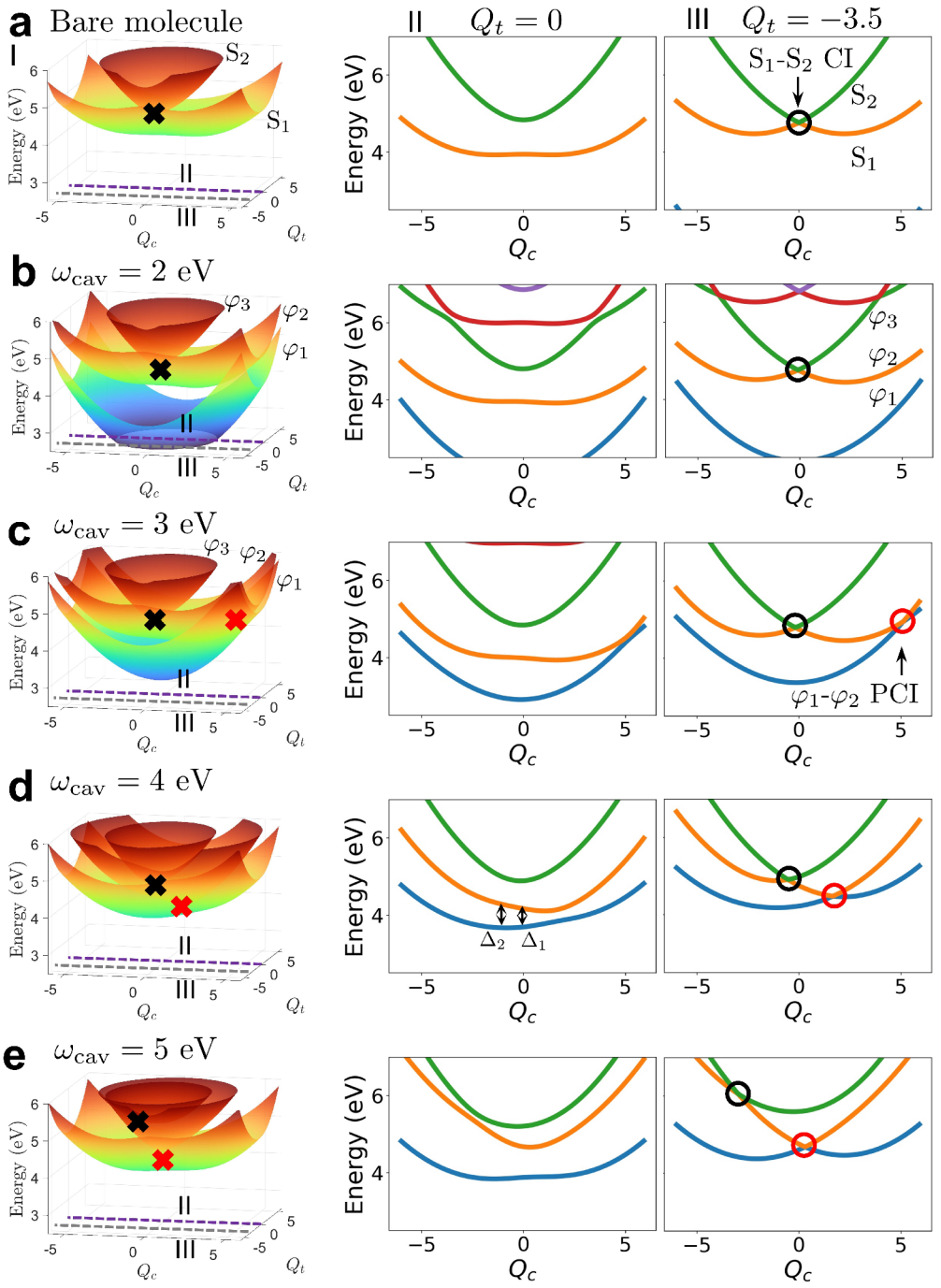

Figure 5. (a) Electronic PES of a bare molecule and (b–e) polaritonic PES (PPES) along the two vibrational coordinates (Q_c and Q_t) at ω_{cav} from 2 to 5 eV (at g = 2000 cm^{-1}) (left panel, I) 3D plot of the PESs. 1D cuts of the PPES along Q_c at (middle panel, II) Q_t = 0 and (right panel, III) Q_t = −3.5. A S_1–S_2 CI and a φ_1–φ_2 polaritonic CI (PCI) are marked by black and red circles, respectively. In panel e, the S_1–S_2 CI becomes also a polaritonic CI. Higher lying polaritonic surfaces that originated from the light–matter interaction between the cavity photon mode and S_1 and S_2 surfaces are shown in (bII) and (bIII).

the conical intersections between S_1 and S_2, can be found at (Q_c, Q_t) = (0.0, −3.6).

When ω_{cav} is increased, the φ_1 surface blue-shifts along with the φ_2 and φ_3 surfaces. This results in a blue-shift in the S_1 band, which is labeled 1 in Figure 4. At ω_{cav} = 3 eV, a new PCI is formed between the φ_1 and φ_2 surfaces at (Q_c, Q_t) = (5.1, −3.5), while keeping the location of S_1–S_2 CI at (Q_c, Q_t) = (−0.6, −3.5). As the PCI is formed, a nonadiabatic electronic transition from φ_2 to φ_1 occurs, resulting in the new PCI band at ω = 3.8 eV when 4.0 eV > ω_{cav}, as shown in Figure 4 marked as 3. The PCI band is only visible at ω_{cav} = 3 eV because the wavepacket on the φ_2 surface cannot reach the φ_1–φ_2 PCI, which is located at a higher energy than the relaxed minimum of the φ_2 surface. The blue-shift of the PCI band at 4.0 eV < ω_{cav} < 5.5 eV indicates that as ω_{cav} increases, the φ_1 surface shifts to higher energy. The observation of these features experimentally may provide direct evidence for the formation of a PCI via molecule–cavity coupling. As the cavity frequency ω_{cav} increases to 5 eV, the φ_1–φ_2 PCI shifts to Q_c = 0 and the S_1–S_2 CI shifts to (Q_c, Q_t) = (−4.5, −3.5). As shown in

https://doi.org/10.1021/jacs.2c00921
J. Am. Chem. Soc. 2022, 144, 7758–7767

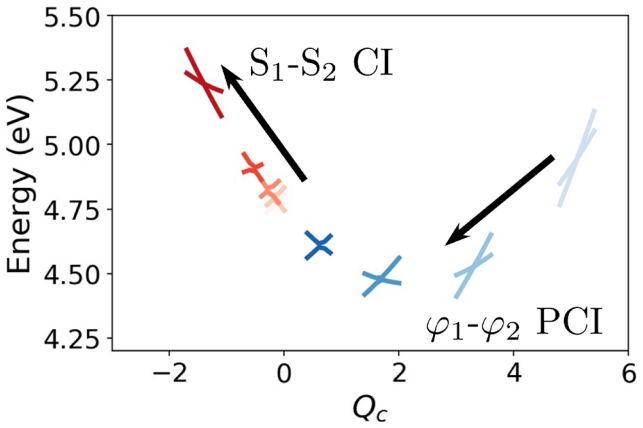

Figure 6. Change in the location of the CI (PCI) as ω_{cav} varies from 3.0 eV (light color) to 4.5 eV (deep color) at 0.5 eV increments (at g = 2000 cm^{-1}). S_1−S_2 CIs and φ_1−φ_2 PCI are colored in red and blue, respectively. Lines represent the shapes of the PPES in the vicinity of the CIs. Black arrows indicate the increase of ω_{cav}.

Supporting Information Figure S2, the locations of the S_1−S_2 CI and φ_1−φ_2 PCI do not change in the Q_t coordinate.

Figure 6 depicts the shift in the location of the S_1−S_2 CI and φ_1−φ_2 PCI as the ω_{cav} increases from 3.0 to 4.5 eV. The CI and PCI shift along the diabatic $B_{2u}(\pi\pi^*)$ state as the other diabatic polaritonic surfaces shift to blue because of the cavity−molecule coupling, while the $B_{2u}(\pi\pi^*)$ surface remains unchanged.

2D Photon Echo Signal of Pyrazine in a Cavity. The 2D photon echo spectra of the bare molecule are compared to those of a molecule coupled to a cavity mode with ω_{cav} = 4 eV at g = 2000 cm^{-1} in Figure 7. 2D signals of bare pyrazine were calculated earlier for similar models.[69−71] This figure also shows the population transfer during the T_2 delay, which is varied between T_2 = 10 and 500 fs. The spectra were obtained by using the phase cycling protocol described in the section Computational Details in the Supporting Information. The wavepacket detected during the T_1 (T_3) time delays causes absorption along the Ω_1 (Ω_3) axis in the 2D spectra. The 2D spectrum of the bare pyrazine molecule is shown in panel (ai). Key signatures are denoted as S_1 and S_2 bands. The diagonal peaks at (Ω_1, Ω_3) = (−4.8, 4.8) eV and (−3.7, 3.7) eV are signatures of the wavepacket created by the initial excitation from S_0 to S_2 and S_1, respectively, which remained on the same surface during T_1 and T_3. Because the transition dipole of the $S_0 \rightarrow S_1$ transition is smaller than that of the $S_0 \rightarrow S_2$ transition, the (Ω_1, Ω_3) = (−3.7, 3.7) eV peak is much weaker than that of the (−4.8, 4.8) eV peak. The cross-peaks at (Ω_1, Ω_3) = (−4.8, 3.7) eV correspond to a wavepacket that is initially promoted from S_0 to S_2 and then decays to S_1. As a result, it provides a signature of the nonadiabatic transition via the conical intersection between S_1 and S_2. The (Ω_1, Ω_3) = (−4.8, 3.0) cross-peaks result from the wavepacket initially created at S_2 and transferred to the S_1 surface at (Q_t, Q_c) = (−3.5, ±2.4) through the S_1−S_2 CI (see Figure 5aIII for the PES). This peak reveals the wavepacket traveling from the S_1−S_2 CI to the bottom of the S_1 surface at (Q_t, Q_c) = (0.0, ±2.2) (see Figure 5aII), which is critical information to determine the population transfer during the dynamics. As the wavepacket fully relaxes to the bottom of the S_1 surface, the peak at (Ω_1, Ω_3) = (−4.8, 3.0) diminishes and the peak at (Ω_1, Ω_3) = (−4.8, 3.7) intensifies as shown in panel (bi).

When a molecule is coupled to a cavity mode, a splitting of the S_1 band into UP and LP in the 2D spectra is observed in panel (bi). Two slightly different splittings can be observed from the 2D spectra, Δ_1 and Δ_2, which are the splittings along the Ω_1 and Ω_3 coordinates, respectively. As shown in Figure 5dii, the Δ_1 and Δ_2 gaps are manifestations of the φ_1−φ_2 gap at the initial absorption occurring at (Q_t, Q_c) = (0.0, 0.0) and relaxed wavepackets at the bottom of the φ_1 surface (Q_t, Q_c) = (0.0, −1.0), respectively.

The population transfer during the nonadiabatic dynamics is reveled by the time delay T_2 dependence of the 2D photon echo signal $S(\Omega_1, T_2, \Omega_3)$. When the two signals $S(\Omega_1, T_2 = 10$ fs, $\Omega_3)$ and $S(\Omega_1, T_2 = 500$ fs, $\Omega_3)$ are compared, it is discovered that the S_1 band at (Ω_1, Ω_3) = (−4.8, 3.8) is significantly enhanced as the population transfers from the S_2 to S_1 surface. Simultaneously, the band at (Ω_1, Ω_3) = (−4.8, 3.2) diminishes as the population transfer nears completion at T_2 = 500 fs (panels bi and di).

The zoomed-in, black boxed region in Figure 7 highlights the time evolution of the wavepacket that was initially prepared on the S_2 surface. Wavepackets transferring from S_2 to S_1($1^{(\prime)}$), wavepackets on S_1 ($2^{(\prime)}$), and wavepackets transferring from φ_2 to φ_1 ($3^{(\prime)}$) are marked as key features. As the population time T_2 is increased, region 2 grows as 1 diminishes in a bare molecule (panels aii and bii), whereas region 2′ grows as 3′ diminishes in a molecule in a cavity (panels cii and dii). The fine structure created by the vibrational progression at region $2^{(\prime)}$ intensifies as T_2 increases. As T_2 changes from 10 to 500 fs, the 2D signal intensity of the peaks $2^{(\prime)}$ and $3^{(\prime)}$ decreased by 40% as the electronic coherences are lost.

We observed valuable extra information from the 2D spectra as compared to the 1D spectra such as population transfer during the dynamics, relaxation of the excited wavepacket on the PPESs, a splitting between polaritonic states, and how a molecule−cavity coupling manipulates the nonadiabatic dynamics. These insights can be used to design and analyze a cavity-modified photochemistry of a system.

CONCLUSIONS

We used the phase-cycling protocol in conjunction with quantum wavepacket dynamics to investigate the effect of optical cavity coupling in the nonadiabatic dynamics of photoexcited pyrazine by computing population dynamics, PPESs, the absorption spectrum, and photon echo signals at different cavity−molecule coupling parameter regimes. We observe the emergence of a novel PCI between the electronic and photonic surfaces as the cavity frequency is tuned. The absorption spectra and third-order photon echo signals capture the formation of a novel PCI and its signatures in the polaritonic dynamics. An experimental observation of these spectral features should provide direct evidence of the formation of the PCI. Other spectroscopic signals including photonic decay, vibrational relaxation, and electronic decoherence can be simulated using our computational protocol. For many molecules, the PCIs also occur in the collective polaritonic surfaces, as illustrated for the case of two molecules.[21] Nevertheless, there are complications due to the collective dark states. The collective dynamics will be determined by the competition between nuclear dynamics on the polaritonic surfaces and relaxation to the dark states.[35]

https://doi.org/10.1021/jacs.2c00921
J. Am. Chem. Soc. 2022, 144, 7758−7767

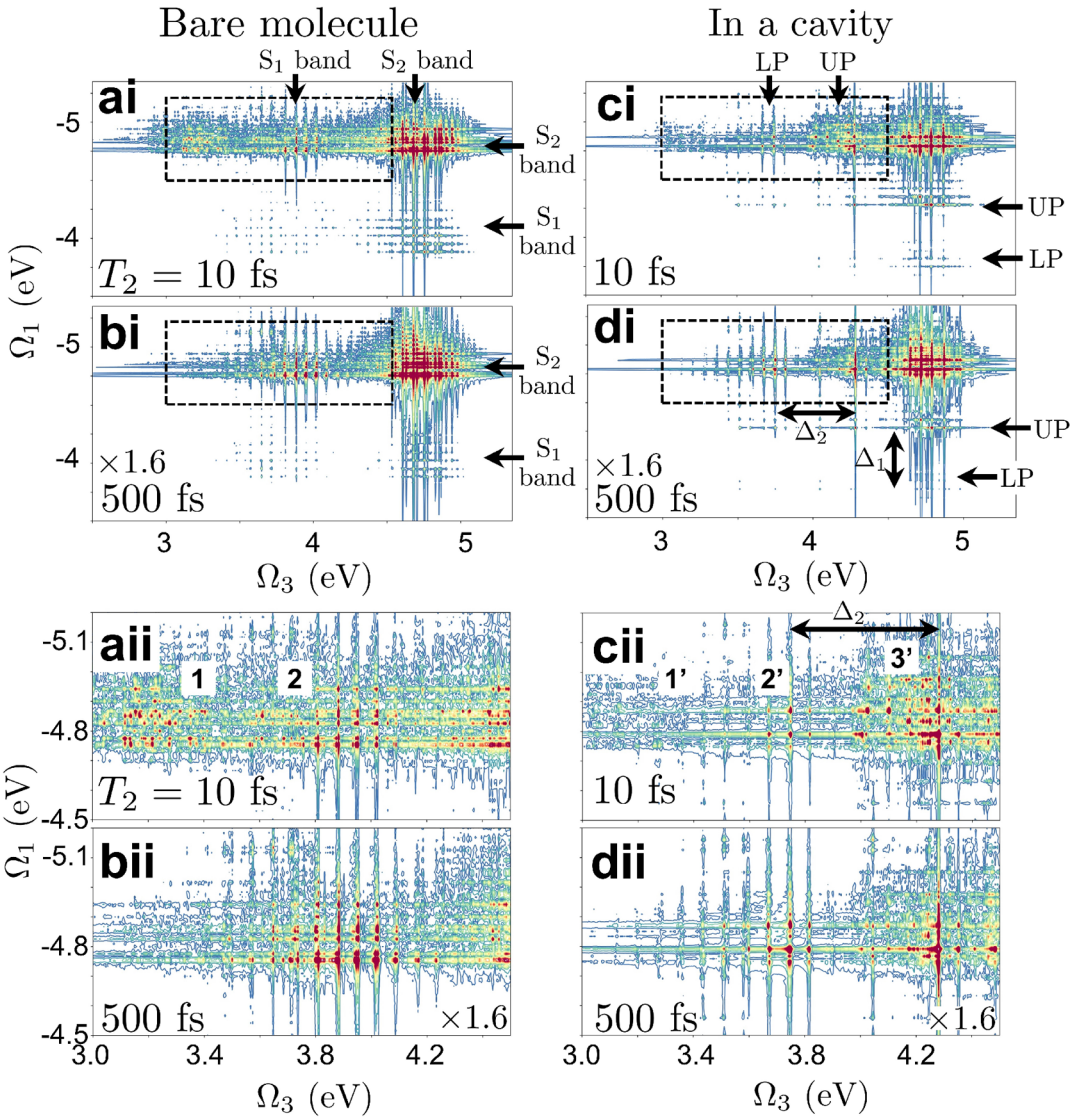

Figure 7. (ai–di) Simulated 2D photon echo spectra $S(\Omega_1, T_2, \Omega_3)$ (eq 8) of (left) a bare molecule and (right) a molecule in a cavity mode with ω_{cav} = 4 eV and coupling strength g = 2000 cm^{-1}. The spectra are simulated at (top) T_2 = 10 fs and (bottom) T_2 = 500 fs. S_1 and S_2 bands are marked. The S_1 band splits into upper (UP) and lower polariton (LP) modes. Separations due to the molecule–cavity coupling (Δ_1 and Δ_2) are clearly visible when compared to the bare molecule case. (aii–dii) Zoomed-in view of the black-boxed region, which amplifies the time evolution of the wavepacket initially prepared on the S_2 surface. Key regions are marked as $1^{(\prime)}$, $2^{(\prime)}$, and $3^{(\prime)}$.

■ ASSOCIATED CONTENT

Supporting Information

The Supporting Information is available free of charge at https://pubs.acs.org/doi/10.1021/jacs.2c00921.

(1) Phase cycling protocol for four-wave mixing signals; (2) supplementary figure for the energy gap between electronic (polaritonic) surfaces along the two vibrational coordinates (Figure S2) (PDF)

■ AUTHOR INFORMATION

Corresponding Authors

Daeheum Cho − *Department of Chemistry and Green-Nano Materials Research Center, Kyungpook National University, Daegu 41566, South Korea;* orcid.org/0000-0002-0322-4291; Email: daeheumc@knu.ac.kr

Bing Gu − *Department of Chemistry and Physics and Astronomy, University of California, Irvine, California 92697-2025, United States;* orcid.org/0000-0002-5787-3334; Email: bingg@uci.edu

Shaul Mukamel − *Department of Chemistry and Physics and Astronomy, University of California, Irvine, California 92697-2025, United States;* orcid.org/0000-0002-6015-3135; Email: smukamel@uci.edu

Complete contact information is available at: https://pubs.acs.org/10.1021/jacs.2c00921

Notes

The authors declare no competing financial interest.

■ ACKNOWLEDGMENTS

The support of the National Science Foundation (Grant No CHE-1953045) and the Chemical Sciences, Geosciences, and Biosciences division, Office of Basic Energy Sciences, Office of Science, U.S. Department of Energy, through Award Nos. DE-FG02-04ER15571 (S.M.) and DE-SC0022134 (B.G.), is

gratefully acknowledged. This work was supported by the National Research Foundation of Korea (NRF) grant funded by the Korea government (MSIT) (No. 2021R1C1C2007977). This work was supported by the National Supercomputing Center with supercomputing resources including technical support (KSC-2021-CRE-0187) (D.C.).

REFERENCES

(1) Kowalewski, M.; Bennett, K.; Mukamel, S. Cavity Femtochemistry: Manipulating Nonadiabatic Dynamics at Avoided Crossings. *J. Phys. Chem. Lett.* **2016**, *7*, 2050.
(2) Bennett, K.; Kowalewski, M.; Mukamel, S. Novel Photochemistry of Molecular Polaritons in Optical Cavities. *Faraday Discuss.* **2016**, *194*, 259−282.
(3) Ebbesen, T. W. Hybrid Light−Matter States in a Molecular and Material Science Perspective. *Acc. Chem. Res.* **2016**, *49*, 2403−2412.
(4) Schäfer, C.; Ruggenthaler, M.; Appel, H.; Rubio, A. Modification of Excitation and Charge Transfer in Cavity Quantum-Electrodynamical Chemistry. *Proc. Natl. Acad. Sci. U.S.A.* **2019**, *116*, 4883−4892.
(5) Galego, J.; Garcia-Vidal, F. J.; Feist, J. Cavity-Induced Modifications of Molecular Structure in the Strong-Coupling Regime. *Phys. Rev. X* **2015**, *5*, No. 041022.
(6) Shalabney, A.; George, J.; Hutchison, J.; Pupillo, G.; Genet, C.; Ebbesen, T. W. Coherent Coupling of Molecular Resonators with a Microcavity Mode. *Nat. Commun.* **2015**, *6*, 5981.
(7) Flick, J.; Narang, P. Cavity-Correlated Electron-Nuclear Dynamics from First Principles. *Phys. Rev. Lett.* **2018**, *121*, 113002.
(8) Herrera, F.; Spano, F. C. Cavity-Controlled Chemistry in Molecular Ensembles. *Phys. Rev. Lett.* **2016**, *116*, 238301.
(9) Coles, D. M.; Somaschi, N.; Michetti, P.; Clark, C.; Lagoudakis, P. G.; Savvidis, P. G.; Lidzey, D. G. Polariton-Mediated Energy Transfer between Organic Dyes in a Strongly Coupled Optical Microcavity. *Nat. Mater.* **2014**, *13*, 712−719.
(10) Frisk Kockum, A.; Miranowicz, A.; De Liberato, S.; Savasta, S.; Nori, F. Ultrastrong Coupling between Light and Matter. *Nat. Rev. Phys.* **2019**, *1*, 19−40.
(11) Vasa, P.; Lienau, C. Strong Light−Matter Interaction in Quantum Emitter/Metal Hybrid Nanostructures. *ACS Photonics* **2018**, *5*, 2−23.
(12) Hertzog, M.; Wang, M.; Mony, J.; Börjesson, K. Strong Light−Matter Interactions: A New Direction within Chemistry. *Chem. Soc. Rev.* **2019**, *48*, 937−961.
(13) Hutchison, J. A.; Schwartz, T.; Genet, C.; Devaux, E.; Ebbesen, T. W. Modifying Chemical Landscapes by Coupling to Vacuum Fields. *Angew. Chem., Int. Ed.* **2012**, *51*, 1592−1596.
(14) Flick, J.; Ruggenthaler, M.; Appel, H.; Rubio, A. Atoms and Molecules in Cavities, from Weak to Strong Coupling in Quantum-Electrodynamics (QED) Chemistry. *Proc. Natl. Acad. Sci. U. S. A.* **2017**, *114*, 3026−3034.
(15) Schwartz, T.; Hutchison, J. A.; Léonard, J.; Genet, C.; Haacke, S.; Ebbesen, T. W. Polariton Dynamics under Strong Light−Molecule Coupling. *ChemPhysChem* **2013**, *14*, 125−131.
(16) Herrera, F.; Spano, F. C. Dark Vibronic Polaritons and the Spectroscopy of Organic Microcavities. *Phys. Rev. Lett.* **2017**, *118*, 223601.
(17) Martínez-Martínez, L. A.; Du, M.; Ribeiro, R.; Kéna-Cohen, S.; Yuen-Zhou, J. Polariton-Assisted Singlet Fission in Acene Aggregates. *J. Phys. Chem. Lett.* **2018**, *9*, 1951−1957.
(18) Sanvitto, D.; Kéna-Cohen, S. The Road towards Polaritonic Devices. *Nat. Mater.* **2016**, *15*, 1061−1073.
(19) Gu, B.; Mukamel, S. Manipulating Two-Photon-Absorption of Cavity Polaritons by Entangled Light. *J. Phys. Chem. Lett.* **2020**, *11*, 8177−8182.
(20) Gu, B.; Mukamel, S. Manipulating Nonadiabatic Conical Intersection Dynamics by Optical Cavities. *Chem. Sci.* **2020**, *11*, 1290−1298.
(21) Gu, B.; Mukamel, S. Cooperative Conical Intersection Dynamics of Two Pyrazine Molecules in an Optical Cavity. *J. Phys. Chem. Lett.* **2020**, *11*, 5555−5562.
(22) Yang, K. Y.; Oh, D. Y.; Lee, S. H.; Yang, Q.-F.; Yi, X.; Shen, B.; Wang, H.; Vahala, K. Bridging Ultrahigh- Q Devices and Photonic Circuits. *Nat. Photonics* **2018**, *12*, 297−302.
(23) Purcell, E. M. Spontaneous Emission Probabilities at Radio Frequencies. *Phys. Rev.* **1946**, *69*, 681.
(24) Zhong, X.; Chervy, T.; Zhang, L.; Thomas, A.; George, J.; Genet, C.; Hutchison, J. A.; Ebbesen, T. W. Energy Transfer between Spatially Separated Entangled Molecules. *Angew. Chem., Int. Ed.* **2017**, *56*, 9034−9038.
(25) George, J.; Shalabney, A.; Hutchison, J. A.; Genet, C.; Ebbesen, T. W. Liquid-Phase Vibrational Strong Coupling. *J. Phys. Chem. Lett.* **2015**, *6*, 1027−1031.
(26) Benz, F.; Schmidt, M. K.; Dreismann, A.; Chikkaraddy, R.; Zhang, Y.; Demetriadou, A.; Carnegie, C.; Ohadi, H.; de Nijs, B.; Esteban, R.; Aizpurua, J.; Baumberg, J. J. Single-Molecule Optomechanics in "Picocavities. *Science* **2016**, *354*, 726−729.
(27) Zhong, X.; Chervy, T.; Wang, S.; George, J.; Thomas, A.; Hutchison, J. A.; Devaux, E.; Genet, C.; Ebbesen, T. W. Non-Radiative Energy Transfer Mediated by Hybrid Light-Matter States. *Angew. Chem.* **2016**, *128*, 6310−6314.
(28) Suzuki, M.; Nishiyama, K.; Kani, N.; Funahashi, M.; Nakanishi, S.; Tsurumachi, N. Dual-Colour Pump-Probe Spectroscopy to Observe the Transition between Polariton Branches in an Ultrastrongly Coupled Microcavity Containing Organic Dye Molecules. *Jpn. J. Appl. Phys.* **2020**, *59*, SCCA08.
(29) Chikkaraddy, R.; de Nijs, B.; Benz, F.; Barrow, S. J.; Scherman, O. A.; Rosta, E.; Demetriadou, A.; Fox, P.; Hess, O.; Baumberg, J. J. Single-Molecule Strong Coupling at Room Temperature in Plasmonic Nanocavities. *Nature* **2016**, *535*, 127−130.
(30) Du, M.; Ribeiro, R. F.; Yuen-Zhou, J. Remote Control of Chemistry in Optical Cavities. *Chem.* **2019**, *5*, 1167−1181.
(31) Gu, B.; Mukamel, S. Optical-Cavity Manipulation of Conical Intersections and Singlet Fission in Pentacene Dimers. *J. Phys. Chem. Lett.* **2021**, *12*, 2052−2056.
(32) Orgiu, E.; George, J.; Hutchison, J. A.; Devaux, E.; Dayen, J. F.; Doudin, B.; Stellacci, F.; Genet, C.; Schachenmayer, J.; Genes, C.; Pupillo, G.; Samorì, P.; Ebbesen, T. W. Conductivity in Organic Semiconductors Hybridized with the Vacuum Field. *Nat. Mater.* **2015**, *14*, 1123−1129.
(33) Thomas, A.; Lethuillier-Karl, L.; Nagarajan, K.; Vergauwe, R. M. A.; George, J.; Chervy, T.; Shalabney, A.; Devaux, E.; Genet, C.; Moran, J.; Ebbesen, T. W. Tilting a Ground-State Reactivity Landscape by Vibrational Strong Coupling. *Science* **2019**, *363*, 615−619.
(34) Xiang, B.; Ribeiro, R. F.; Du, M.; Chen, L.; Yang, Z.; Wang, J.; Yuen-Zhou, J.; Xiong, W. Intermolecular Vibrational Energy Transfer Enabled by Microcavity Strong Light−Matter Coupling. *Science* **2020**, *368*, 665−667.
(35) Ulusoy, I. S.; Gomez, J. A.; Vendrell, O. Modifying the Nonradiative Decay Dynamics through Conical Intersections via Collective Coupling to a Cavity Mode. *J. Phys. Chem. A* **2019**, *123*, 8832−8844.
(36) Ribeiro, R. F.; Martínez-Martínez, L. A.; Du, M.; Campos-Gonzalez-Angulo, J.; Yuen-Zhou, J. Polariton Chemistry: Controlling Molecular Dynamics with Optical Cavities. *Chem. Sci.* **2018**, *9*, 6325−6339.
(37) Du, M.; A. Martínez-Martínez, L.; R. Ribeiro, F.; Hu, Z.; M. Menon, V.; Yuen-Zhou, J. Theory for Polariton-Assisted Remote Energy Transfer. *Chem. Sci.* **2018**, *9*, 6659−6669.
(38) Zhang, Y.; Nelson, T.; Tretiak, S. Non-Adiabatic Molecular Dynamics of Molecules in the Presence of Strong Light-Matter Interactions. *J. Chem. Phys.* **2019**, *151*, 154109.
(39) Sun, S.; Gu, B.; Mukamel, S. Polariton ring currents and circular dichroism of Mg-porphyrin in a chiral cavity. *Chem. Sci.* **2022**, *13*, 1037−1048.

https://doi.org/10.1021/jacs.2c00921
J. Am. Chem. Soc. 2022, 144, 7758−7767

(40) Domcke, W.; Yarkony, D. R.; Köppel, H. *Conical Intersections: Theory, Computation and Experiment*; World Scientific, 2011.
(41) Lim, J. S.; Kim, S. K. Experimental probing of conical intersection dynamics in the photodissociation of thioanisole. *Nat. Chem.* **2010**, *2*, 627−632.
(42) You, H. S.; Han, S.; Lim, J. S.; Kim, S. K. ($\pi\pi^*/\pi\sigma^*$) Conical Intersection Seam Experimentally Observed in the S−D Bond Dissociation Reaction of Thiophenol-d_1. *J. Phys. Chem. Lett.* **2015**, *6*, 3202−3208.
(43) Musser, A. J.; Liebel, M.; Schnedermann, C.; Wende, T.; Kehoe, T. B.; Rao, A.; Kukura, P. Evidence for conical intersection dynamics mediating ultrafast singlet exciton fission. *Nat. Phys.* **2015**, *11*, 352−357.
(44) Worner, H. J.; Bertrand, J. B.; Fabre, B.; Higuet, J.; Ruf, H.; Dubrouil, A.; Patchkovskii, S.; Spanner, M.; Mairesse, Y.; Blanchet, V.; Mevel, E.; Constant, E.; Corkum, P. B.; Villeneuve, D. M. Conical Intersection Dynamics in NO2 Probed by Homodyne High-Harmonic Spectroscopy. *Science* **2011**, *334*, 208−212.
(45) Horio, T.; Fuji, T.; Suzuki, Y.-I.; Suzuki, T. Probing Ultrafast Internal Conversion through Conical Intersection via Time-Energy Map of Photoelectron Angular Anisotropy. *J. Am. Chem. Soc.* **2009**, *131*, 10392−10393.
(46) Hoffman, D. P.; Ellis, S. R.; Mathies, R. A. Characterization of a Conical Intersection in a Charge-Transfer Dimer with Two-Dimensional Time-Resolved Stimulated Raman Spectroscopy. *J. Phys. Chem. A* **2014**, *118*, 4955−4965.
(47) Hoffman, D. P.; Mathies, R. A. Femtosecond Stimulated Raman Exposes the Role of Vibrational Coherence in Condensed-Phase Photoreactivity. *Acc. Chem. Res.* **2016**, *49*, 616−625.
(48) Polli, D.; Altoè, P.; Weingart, O.; Spillane, K. M.; Manzoni, C.; Brida, D.; Tomasello, G.; Orlandi, G.; Kukura, P.; Mathies, R. A.; Garavelli, M.; Cerullo, G. Conical intersection dynamics of the primary photoisomerization event in vision. *Nature* **2010**, *467*, 440−443.
(49) McFarland, B. K.; et al. Ultrafast X-ray Auger probing of photoexcited molecular dynamics. *Nat. Commun.* **2014**, *5*, 4235.
(50) Raab, A.; Worth, G. A.; Meyer, H.-D.; Cederbaum, L. S. Molecular dynamics of pyrazine after excitation to the S2 electronic state using a realistic 24-mode model Hamiltonian. *J. Chem. Phys.* **1999**, *110*, 936−946.
(51) Oliver, T. A. A.; Lewis, N. H. C.; Fleming, G. R. Correlating the motion of electrons and nuclei with two-dimensional electronic-vibrational spectroscopy. *Proc. Natl. Acad. Sci. U.S.A.* **2014**, *111*, 10061−10066.
(52) Timmers, H.; Li, Z.; Shivaram, N.; Santra, R.; Vendrell, O.; Sandhu, A. Coherent Electron Hole Dynamics Near a Conical Intersection. *Phys. Rev. Lett.* **2014**, *113*, 113003.
(53) Kowalewski, M.; Mukamel, S. Stimulated Raman signals at conical intersections: Ab initio surface hopping simulation protocol with direct propagation of the nuclear wave function. *J. Chem. Phys.* **2015**, *143*, No. 044117.
(54) von Conta, A.; Tehlar, A.; Schletter, A.; Arasaki, Y.; Takatsuka, K.; Worner, H. J. Conical-intersection dynamics and ground-state chemistry probed by extreme-ultraviolet time-resolved photoelectron spectroscopy. *Nat. Commun.* **2018**, *9*, 3162.
(55) Kowalewski, M.; Bennett, K.; Dorfman, K. E.; Mukamel, S. Catching Conical Intersections in the Act: Monitoring Transient Electronic Coherences by Attosecond Stimulated X-Ray Raman Signals. *Phys. Rev. Lett.* **2015**, *115*, 193003.
(56) Szidarovszky, T.; Halász, G. J.; Császár, A. G.; Cederbaum, L. S.; Vibók, Á. Conical Intersections Induced by Quantum Light: Field-Dressed Spectra from the Weak to the Ultrastrong Coupling Regimes. *J. Phys. Chem. Lett.* **2018**, *9*, 6215−6223.
(57) Vendrell, O. Coherent Dynamics in Cavity Femtochemistry: Application of the Multi-Configuration Time-Dependent Hartree Method. *Chem. Phys.* **2018**, *509*, 55.
(58) Xiang, B.; Ribeiro, R. F.; Dunkelberger, A. D.; Wang, J.; Li, Y.; Simpkins, B. S.; Owrutsky, J. C.; Yuen-Zhou, J.; Xiong, W. Two-Dimensional Infrared Spectroscopy of Vibrational Polaritons. *Proc. Natl. Acad. Sci. U.S.A.* **2018**, *115*, 4845−4850.
(59) Avramenko, A. G.; Rury, A. S. Local Molecular Probes of Ultrafast Relaxation Channels in Strongly Coupled Metalloporphyrin-Cavity Systems. *J. Chem. Phys.* **2021**, *155*, No. 064702.
(60) Saurabh, P.; Mukamel, S. Two-Dimensional Infrared Spectroscopy of Vibrational Polaritons of Molecules in an Optical Cavity. *J. Chem. Phys.* **2016**, *144*, 124115.
(61) Cho, M. Coherent Two-Dimensional Optical Spectroscopy. *Chem. Rev.* **2008**, *108*, 1331−1418.
(62) Mukamel, S. *Principles of Nonlinear Optical Spectroscopy*; Oxford University Press, 1995.
(63) Seidner, L.; Stock, G.; Sobolewski, A. L.; Domcke, W. Ab Initio Characterization of the S1−S2 Conical Intersection in Pyrazine and Calculation of Spectra. *J. Chem. Phys.* **1992**, *96*, 5298−5309.
(64) Domcke, W., Yarkony, D., Köppel, H., Eds. *Conical Intersections: Electronic Structure, Dynamics & Spectroscopy*; Advanced Series in Physical Chemistry v.15; World Scientific: River Edge, NJ, 2004.
(65) Scheurer, C.; Mukamel, S. Magnetic Resonance Analogies in Multidimensional Vibrational Spectroscopy. *Bull. Chem. Soc. Jpn.* **2002**, *75*, 989−999.
(66) Seidner, L.; Stock, G.; Domcke, W. Nonperturbative approach to femtosecond spectroscopy: General theory and application to multidimensional nonadiabatic photoisomerization processes. *J. Chem. Phys.* **1995**, *103*, 3998−4011.
(67) Gelin, M. F.; Egorova, D.; Domcke, W. Efficient Calculation of Time- and Frequency-Resolved Four-Wave-Mixing Signals. *Acc. Chem. Res.* **2009**, *42*, 1290−1298.
(68) Hamm, P.; Zanni, M. *Concepts and Methods of 2D Infrared Spectroscopy*; Cambridge University Press: Cambridge, 2011.
(69) Krčmář, J.; Gelin, M. F.; Egorova, D.; Domcke, W. Signatures of conical intersections in two-dimensional electronic spectra. *J. Phys. B: At. Mol. Opt. Phys.* **2014**, *47*, 124019.
(70) Krčmář, J.; Gelin, M. F.; Domcke, W. Simulation of femtosecond two-dimensional electronic spectra of conical intersections. *J. Chem. Phys.* **2015**, *143*, No. 074308.
(71) Sun, K.; Xu, Q.; Chen, L.; Gelin, M. F.; Zhao, Y. Temperature effects on singlet fission dynamics mediated by a conical intersection. *J. Chem. Phys.* **2020**, *153*, 194106.

https://doi.org/10.1021/jacs.2c00921
J. Am. Chem. Soc. 2022, 144, 7758−7767

-SUPPORTING INFORMATION-

for

Optical-Cavity Manipulation and Nonlinear UV Molecular Spectroscopy of Conical Intersections in Pyrazine

Daeheum Cho,*,† Bing Gu,*,‡ and Shaul Mukamel*,‡

†*Department of Chemistry and Green-Nano Materials Research Center, Kyungpook National University, Daegu 41566, South Korea*

‡*Department of Chemistry and Physics and Astronomy, University of California, Irvine, California 92697-2025, USA*

E-mail: daeheumc@knu.ac.kr; bingg@uci.edu; smukamel@uci.edu

The Phase Cycling Protocol for Four-wave Mixing Signals

Nonlinear signals are given by sums over Liouville pathways, each of which represents a different sequence of interactions with the fields. Phase matching is a conventional approach to distinguish different nonlinear pathways by employing a noncollinear pulse configuration, and phase cycling is a convenient experimental and computational alternative. Phase cycling protocol employs combinations of collinear pulses with different phases to separate the various pathways. The measurements are repeated for a finite set of phase differences between the incoming pulses $\phi_s = \pm\phi_1 \pm \phi_2 \pm \phi_3$, where ϕ_1, ϕ_2, and ϕ_3 are the incoming field phases. Specific combinations of signals with different polarization configurations can isolate the contributions of different groups of pathways from the total polarization. It requires a phase cycling protocol to sort out the desired nonlinear signal, when the direct time-domain simulation of multidimensional signals of molecules are used to solve the Schrodinger equation nonperturbatively in the external fields. We have employed a 9-step phase cycling protocol to single out the third-order photon echo contribution of pyrazine from the nonadiabatic dynamics driven by three external UV pulses.

In nonlinear FWM spectroscopy, the system interacts with three electric pulses $\mathbf{E}_i(t)$, where $i \in \{1, 2, 3\}$ indicates the order of arrival of the pulses, and is finally detected by the local oscillator field $\mathbf{E}_4(t)$, which interferes with the emitted signal to generate the heterodyne signal. Because the incoming fields are included non-perturbatively in the simulation, nonlinear effects induced by intense external fields can be described.

The heterodyne-detected signal is given by

$$S = \Im \int \mathrm{d}t \langle \boldsymbol{\mu}(t) \rangle \cdot \mathbf{E}_4^*(t). \tag{S1}$$

Further, we show how the third-order contribution and desired pathways can be singled out from the total third-order signal.

$$S^{(3)}(t_3,t_2,t_1) = \int \mathrm{d}t\mathrm{d}t_3\mathrm{d}t_2\mathrm{d}t_1 R^{(3)}(t_3,t_2,t_1) \times \mathbf{E}_4(t)\mathbf{E}_3(t-t_3)\mathbf{E}_2(t-t_3-t_2)\mathbf{E}_1(t-t_3-t_2-t_1) \tag{S2}$$

The third-order response function $R^{(3)}(t_3,t_2,t_1)$ can be expanded in Liouville pathways (see Figure S1 for diagrams)

$$R^{(3)}(t_3,t_2,t_1) = \sum_{n=1}^{6} R_n(t_3,t_2,t_1) + c.c. \tag{S3}$$

Pathways 1, 2, and 3 represent the photon echo signal ($\mathbf{k}_I = -\mathbf{k}_1+\mathbf{k}_2+\mathbf{k}_3$) with phase $\phi_I = -\phi_1+\phi_2+\phi_3-\phi_4$, while 4, 5, and 6 represent non-rephasing signals ($\mathbf{k}_{II} = \mathbf{k}_1-\mathbf{k}_2+\mathbf{k}_3$) with phase $\phi_{II} = \phi_1-\phi_2+\phi_3-\phi_4$. The double quantum coherence signals ($\mathbf{k}_{III} = \mathbf{k}_1+\mathbf{k}_2-\mathbf{k}_3$), which involve doubly excited states, with phase $\phi_{III} = \phi_1+\phi_2-\phi_3-\phi_4$ are not considered in this article.

The entire third-order response can be recast as

$$S^{(3)}(\phi_1,\phi_2,\phi_3,\phi_4) = \sum_{n=1}^{6} e^{i(\pm\phi_1\pm\phi_2\pm\phi_3-\phi_4)} \int \mathrm{d}t\mathrm{d}t_3\mathrm{d}t_2\mathrm{d}t_1 R_n(t_3,t_2,t_1) \times \mathbf{E}_4(t)\mathbf{E}_3(t-t_3)\mathbf{E}_2(t-t_3-t_2)\mathbf{E}_1(t-t_3-t_2-t_1) = \sum_{n=1}^{6} c_n(\phi_1,\phi_2,\phi_3,\phi_4)S_n \tag{S4}$$

where n represents the different Liouville pathways contributing to the following third-order response

$$S_n = \Im \int \mathrm{d}t\mathrm{d}t_3\mathrm{d}t_2\mathrm{d}t_1 R_n(t_3,t_2,t_1)\mathbf{E}_4(t)\mathbf{E}_3(t-t_3)\mathbf{E}_2(t-t_3-t_2)\mathbf{E}_1(t-t_3-t_2-t_1) \tag{S5}$$

and

$$c_1(\phi_1,\phi_2,\phi_3,\phi_4) = e^{i(-\phi_1+\phi_2+\phi_3-\phi_4)}, c_4(\phi_1,\phi_2,\phi_3,\phi_4) = e^{i(\phi_1-\phi_2+\phi_3-\phi_4)}. \tag{S6}$$

The photon echo diagrams, R_1, R_2, and R_3, are defined by their common overall phase $\phi_I = -\phi_1 + \phi_2 + \phi_3 - \phi_4$ and $c_1 = c_2 = c_3$, whereas the non-rephasing diagrams, R_4, R_5, and R_6, have the phase $\phi_{II} = +\phi_1 - \phi_2 + \phi_3 - \phi_4$ and $c_4 = c_5 = c_6$. The photon echo R_I and non-rephasing R_{II} response functions are given by

$$R_I = R_1 + R_2 + R_3, R_{II} = R_4 + R_5 + R_6. \tag{S7}$$

We used a 9-step phase cycling protocol with $\phi_1 = X$, $\phi_2 \in \{X, Y, Z\}$, $\phi_3 \in \{X, Y, Z\}$, and $\phi_4 = X$. Moreover, we can isolate the photon echo $\mathbf{k}_I$ and non-rephasing $\mathbf{k}_{II}$ signals from lower order signals by solving a set of linear equations of the signals listed in Supporting Information Table S1 with a set of phase combinations $\phi_1 = X$, $\phi_2 \in \{X, Y, Z\}$, $\phi_3 \in \{X, Y, Z\}$, and $\phi_4 = X$ (where $X = 0$, $Y = \pi/2$, $Z = \pi$), .By relating the phase cycling coefficients matrix to the total signal with a different set of phase combinations S_{ϕ_1,ϕ_2,ϕ_3}, the real and imaginary parts of photon echo R_I and non-rephasing R_{II} response functions can be obtained (See Supporting Information eq. S8). It should be noted that the phase cycling protocol used here will not eliminate entries 24-29 in Table S1 . Photon echo and non-rephasing components, however, can be distinguished from those entries by the frequency at which they appear. The photon echo and non-rephasing components appear at $\Omega_1 = \omega_1$ and $-\omega_1$, respectively, whereas entries 24-29 appear at $\Omega_1 = 0$ (since there is no coherence during the t_1 delay).

$$\begin{pmatrix} 0 & 0.25 & 0.25 & -0.50 & -0.25 & 0.25 & -0.25 & 0.25 & 0 \\ 0.25 & -0.25 & -0.25 & 0 & 0 & 0.25 & 0 & 0.25 & -0.25 \\ 0.25 & -0.25 & -0.25 & 0.50 & 0 & -0.25 & 0 & -0.25 & 0.25 \\ 0 & -0.25 & 0.25 & 0 & 0.25 & -0.25 & -0.25 & 0.25 & 0 \end{pmatrix} \begin{pmatrix} S_{XXX} \\ S_{XXY} \\ S_{XYX} \\ S_{XYY} \\ S_{XXZ} \\ S_{XYZ} \\ S_{XZX} \\ S_{XZY} \\ S_{XZZ} \end{pmatrix} = \begin{pmatrix} \Re R_I \\ \Im R_I \\ \Re R_{II} \\ \Im R_{II} \end{pmatrix} \tag{S8}$$

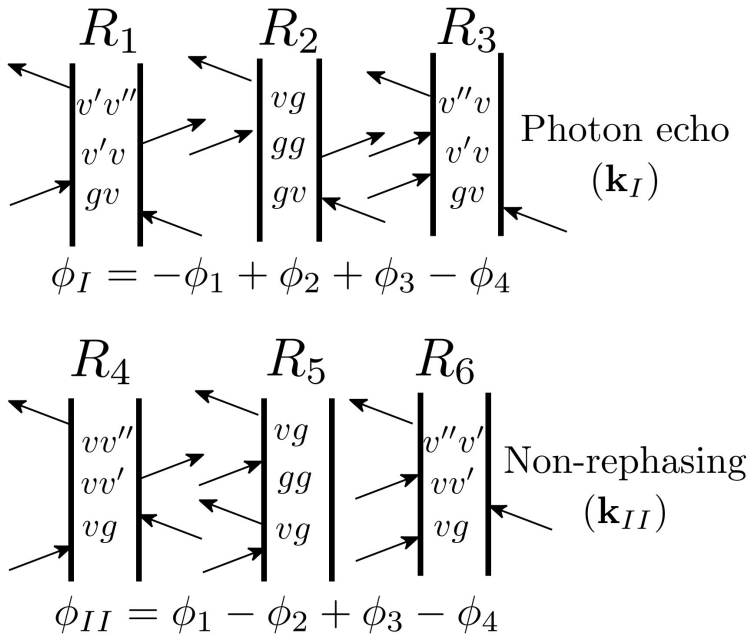

Figure S1: Liouville pathway diagrams for photon echo and non-rephasing pathways.)

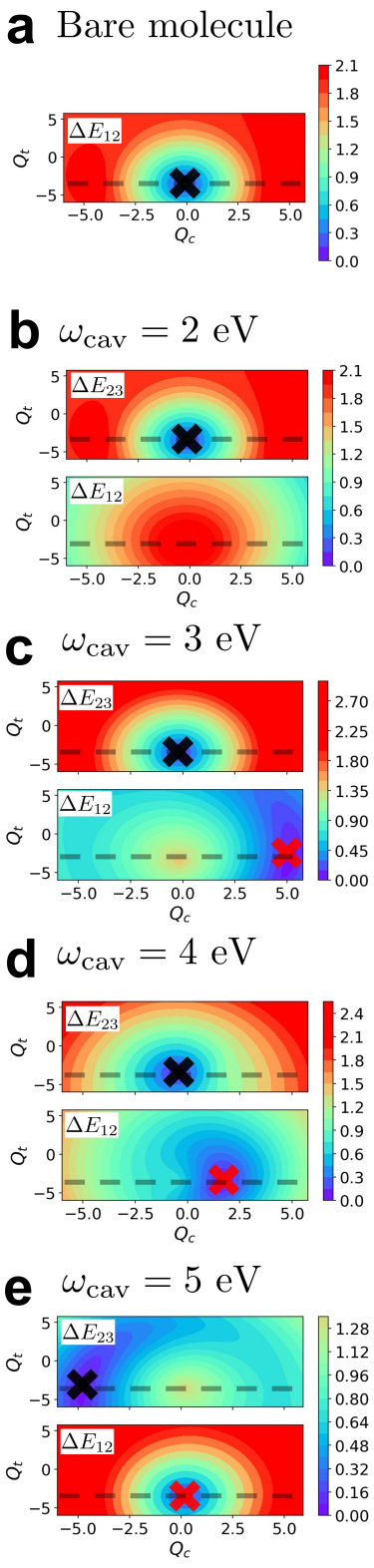

Figure S2: The energy gap between electronic (polaritonic) surfaces along the two vibrational coordinates. (a) the S_1-S_2 gap (ΔE_{12}) of a bare molecule. (b-e) (top) the φ_2-φ_3 gap (ΔE_{23}) and (bottom) φ_1-φ_2 gap (ΔE_{12}) at ω_{cav} from 2 to 5 eV (the cavity coupling strength $g = 2000$ cm^{-1})

Table S1: Phase cycling coefficients for possible signal expressions up to third-order.

index j	$\mathbf{k}_s$	ϕ_1	ϕ_2	ϕ_3
1	$\mathbf{k}_I = -\mathbf{k}_1 + \mathbf{k}_2 + \mathbf{k}_3$	$e^{-i\phi_1}$	$e^{i\phi_2}$	$e^{i\phi_3}$
2	$\mathbf{k}_{II} = \mathbf{k}_1 - \mathbf{k}_2 + \mathbf{k}_3$	$e^{i\phi_1}$	$e^{-i\phi_2}$	$e^{i\phi_3}$
3	$\mathbf{k}_s = \pm\mathbf{k}_1$	$e^{\pm i\phi_1}$	1	1
4	$\mathbf{k}_s = \pm\mathbf{k}_2$	1	$e^{\pm i\phi_2}$	1
5	$\mathbf{k}_s = \pm\mathbf{k}_3$	1	1	$e^{\pm i\phi_3}$
6	$\mathbf{k}_s = \pm 2\mathbf{k}_1$	$e^{\pm 2i\phi_1}$	1	1
7	$\mathbf{k}_s = \pm 2\mathbf{k}_2$	1	$e^{\pm 2i\phi_2}$	1
8	$\mathbf{k}_s = \pm 2\mathbf{k}_3$	1	1	$e^{\pm 2i\phi_3}$
9	$\mathbf{k}_s = \pm 3\mathbf{k}_1$	$e^{\pm 3i\phi_1}$	1	1
10	$\mathbf{k}_s = \pm 3\mathbf{k}_2$	1	$e^{\pm 3i\phi_2}$	1
11	$\mathbf{k}_s = \pm 3\mathbf{k}_3$	1	1	$e^{\pm 3i\phi_3}$
12	$\mathbf{k}_s = \pm\mathbf{k}_1 \mp \mathbf{k}_2$	$e^{\pm i\phi_1}$	$e^{\mp i\phi_2}$	1
13	$\mathbf{k}_s = \pm\mathbf{k}_1 \pm \mathbf{k}_2$	$e^{\pm i\phi_1}$	$e^{\pm i\phi_2}$	1
14	$\mathbf{k}_s = \pm\mathbf{k}_1 \pm \mathbf{k}_3$	$e^{\pm i\phi_1}$	1	$e^{\pm i\phi_3}$
15	$\mathbf{k}_s = \pm\mathbf{k}_1 \mp \mathbf{k}_3$	$e^{\pm i\phi_1}$	1	$e^{\mp i\phi_3}$
16	$\mathbf{k}_s = \pm 2\mathbf{k}_1 \pm \mathbf{k}_2$	$e^{\pm 2i\phi_1}$	$e^{\pm i\phi_2}$	1
17	$\mathbf{k}_s = \pm 2\mathbf{k}_1 \mp \mathbf{k}_2$	$e^{\pm 2i\phi_1}$	$e^{\mp i\phi_2}$	1
18	$\mathbf{k}_s = \pm 2\mathbf{k}_1 \pm \mathbf{k}_3$	$e^{\pm 2i\phi_1}$	1	$e^{\pm i\phi_3}$
19	$\mathbf{k}_s = \pm 2\mathbf{k}_1 \mp \mathbf{k}_3$	$e^{\pm 2i\phi_1}$	1	$e^{\mp i\phi_3}$
20	$\mathbf{k}_s = \pm\mathbf{k}_1 \pm 2\mathbf{k}_2$	$e^{\pm i\phi_1}$	1	$e^{\pm 2i\phi_2}$
21	$\mathbf{k}_s = \pm\mathbf{k}_1 \mp 2\mathbf{k}_2$	$e^{\pm i\phi_1}$	1	$e^{\mp 2i\phi_2}$
22	$\mathbf{k}_s = \pm\mathbf{k}_1 \pm 2\mathbf{k}_3$	$e^{\pm i\phi_1}$	1	$e^{\pm 2i\phi_3}$
23	$\mathbf{k}_s = \pm\mathbf{k}_1 \mp 2\mathbf{k}_3$	$e^{\pm i\phi_1}$	1	$e^{\mp 2i\phi_3}$
24	$\mathbf{k}_s = \pm\mathbf{k}_2 \pm \mathbf{k}_3$	1	$e^{\pm i\phi_2}$	$e^{\pm i\phi_3}$
25	$\mathbf{k}_s = \pm\mathbf{k}_2 \mp \mathbf{k}_3$	1	$e^{\pm i\phi_2}$	$e^{\mp i\phi_3}$
26	$\mathbf{k}_s = \pm 2\mathbf{k}_2 \pm \mathbf{k}_3$	1	$e^{\pm 2i\phi_2}$	$e^{\pm i\phi_3}$
27	$\mathbf{k}_s = \pm 2\mathbf{k}_2 \mp \mathbf{k}_3$	1	$e^{\pm 2i\phi_2}$	$e^{\mp i\phi_3}$
28	$\mathbf{k}_s = \pm\mathbf{k}_2 \mp 2\mathbf{k}_3$	1	$e^{\pm i\phi_2}$	$e^{\mp 2i\phi_3}$
29	$\mathbf{k}_s = \pm\mathbf{k}_2 \mp 2\mathbf{k}_3$	1	$e^{\pm i\phi_2}$	$e^{\mp 2i\phi_3}$